Combined experimental–numerical study on residual stresses induced by a single impact as elementary process of mechanical peening

Sandmann, Paul; Nielsen, Marc André; Keller, Sören; Maawad, Emad; Staron, Peter; Klusemann, Benjamin

Published in:
Strain

DOI:
10.1111/str.12338

Publication date:
2020

Document Version
Publisher's PDF, also known as Version of record

Received: 6 May 2019 | Revised: 20 November 2019 | Accepted: 8 February 2020

DOI: 10.1111/str.12338

FULL PAPER

WILEY strain

Combined experimental–numerical study on residual stresses induced by a single impact as elementary process of mechanical peening

Paul Sandmann[1] | **Marc-André Nielsen**[2] | **Sören Keller**[2] | **Emad Maawad**[2] | **Peter Staron**[2] | **Benjamin Klusemann**[1,2]

[1]Institute of Product and Process Innovation, Leuphana University of Lüneburg, Lüneburg, Germany

[2]Institute of Materials Research, Helmholtz-Zentrum Geesthacht, Geesthacht, Germany

Correspondence
Paul Sandmann, Leuphana University of Lüneburg, Lüneburg, Germany.
Email: paul.sandmann@icloud.com

Present address
Paul Sandmann, Department of Mechanical Engineering, Imperial College London, Exhibition Road, London SW7 2AZ, UK.

Abstract

Peening processes can be used as a fatigue enhancement treatment for metallic structures by locally introducing compressive residual stresses. A combined experimental–numerical study on a single-impact process with a drop tower on the aluminium alloy AA5754, representing the elementary process of mechanical peening, has been performed to investigate different impact parameters on the residual stress profile. Residual stresses have been measured using high-energy X-Ray diffraction. A three-dimensional finite element model is used to predict the residual stresses numerically. The elastic strain components from the numerical results are used to calculate residual stresses by assuming either a plane stress or a plane strain state for different specimen thickness to assess the validity of respective assumption. The validity of the numerical simulation is evaluated based on comparisons of the elastic strain profiles and the percentage loss in kinetic energy of the steel ball due to the impact for four different energies, showing overall a good agreement in the experimental–numerical comparisons.

KEYWORDS

aluminium alloys, elementary peening process, finite element analysis, residual stress, single mechanical impact, X-ray diffraction

1 | INTRODUCTION

A major challenge for, for example, aircraft or automotive industries is to find practical and efficient strategies for maintaining and increasing the fatigue life of highly stressed metallic structures. In this context, promising and cost-effective solutions are provided by residual-stress-based approaches using peening processes like hammer peening, shot peening, laser shock peening, or ultrasonic impact treatment.[1–4] Generally, these processes rely on the same principle: inducing compressive residual stress to prevent or inhibit the crack propagation, which should lead to an increase in the fatigue life.[5] However, the induction of compressive stresses always comes with balancing tensile stresses, which, if present at critical positions, might lead components to prematurely crack and consequently to have shorter lifespan.[6] It is therefore required to know the distribution of residual stresses to assess their effect on the fatigue life and finally to determine the optimal peening strategy to gain the maximum fatigue improvement. In the current study, the aluminium alloy AA5754 is investigated which is highly used within the automotive industry where mild steel in automobile bodies is replaced by

such an alloy due to its superior material properties of, for example, low density, high specific strengths and corrosion resistance.[7]

In recent years, (multi-impact) shot peening, ultrasonic peening, or laser shock peening models have been investigated by several researchers.[8–13] In contrast, single-impact models are rarely reported. Boyce et al.[14] investigated the residual stresses caused by a spherical projectile impacting upon a flat surface to investigate the reduction in component lifetime due to foreign object damage. A quasi-static and dynamic numerical model of a spherical hard body impact for Ti-6Al-4V using an axisymmetric approach were compared with X-ray diffraction measurements. Tensile residual stresses on the surface along the loading axis as well as compressive stresses directly beneath the impact area were reported. However, considering an impact pattern, the tensile residual stresses at the surface are smaller after multiple impacts.[15,16] The study of Xiao et al.[16] focused on developing a numerical dynamic shot peening model with single and repeated impact to obtain stresses at different peening stages. It was demonstrated that the depth of compressive residual stresses increases with increasing number of impacts at the same location, while the maximum value of compressive stress was observed to increase only slightly. Guo et al.[15] revealed the residual stress distributions produced by ultrasonic impact treatment using a single-impact model validated by experimentally obtained indentations. The effect of a second impact was investigated as well. Especially the pin velocity was found to have a significant impact on the maximum compressive residual stresses.

This paper aims at studying the residual stress profiles induced by a single impact, representing the elementary process of mechanical peening, via a combined experimental–numerical approach. High-energy X-ray diffraction measurements have been used in combination with a finite element (FE) model to investigate the residual stress distribution.

2 | EXPERIMENTAL SET-UP

2.1 | Single impact experiments via drop tower

A band saw including subsequent milling was used to cut specimens from AA5754 aluminium sheets in annealed and recrystallized (H111) condition. A microstructural characterization of the material used is, for example, presented by Froend et al.[17] The chemical composition of AA5754 is given in Table 1. Specimens with a size of 40 × 25 × 3 mm were cut from the sheet material. The specimens were subjected to a single-impact event on the surface normal to the cut by a steel ball with a diameter of 25 mm and a weight of 63.67 g at energy levels defined via the gravitational potential energy, that is, 0.25, 0.5, 0.75, and 1 J, assuming energy conservation. This leads to impact velocities ranging from 10 to 20 km/hr. The experimental set-up for the single-impact test is shown in Figure 1b. The sample was clamped at the lower end of the drop tower, see Figure 1c. The sample was clamped only at the bottom edge; thus, the clamping forces do not interfere

TABLE 1 Chemical composition of AA5754 (in wt%)[17]

Composition	Si	Fe	Cu	Mn	Mg	Cr	Zn	Zr	Ti	Al
wt%	≤0.40	≤0.40	≤0.10	≤0.50	2.60-3.60	≤0.30	≤0.20	≤0.15	≤0.15	Bal.

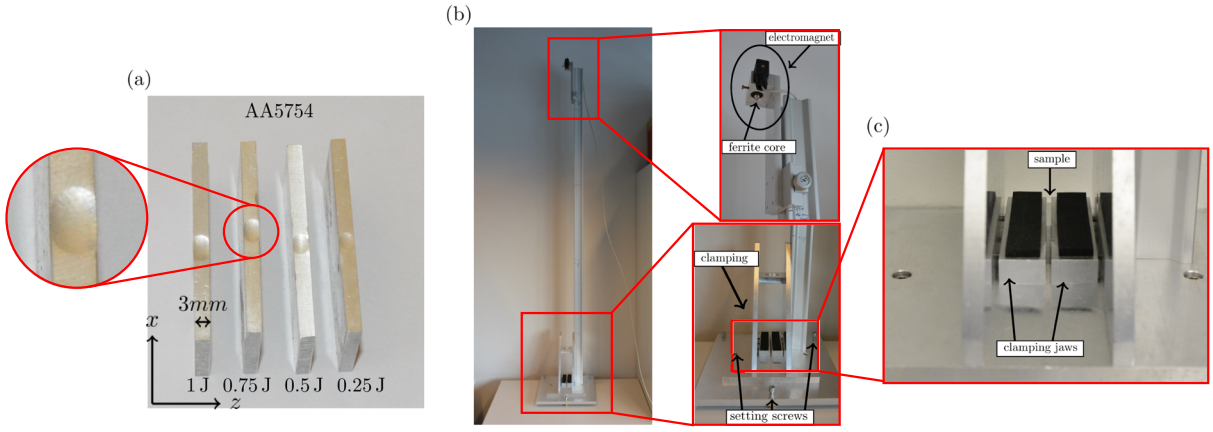

FIGURE 1 (a) Single impact specimens of aluminium alloy AA5754. Peening with lower energy lead to a shallower and smaller indentation shape. (b) Experimental set-up of the single-impact process. The ball is dropped from a specific height, corresponding to a respective energy level (0.25, 0.5, 0.75, and 1 J). (c) Close up of the clamping used to fix the specimen during the single impact

with the elasto-plastic impact zone on the upper edge. The ball was initially fixed to the top of the drop tower via an electromagnet, allowing to precisely and repeatably hit the specimen without any rotation of the ball. At the time of the impact, a force is exerted on the specimen for a relatively short time, determined by the impact energy. Consequently, plastic and elastic deformation are resulting in the specimen. Specimens after single impacts are depicted in Figure 1a.

2.2 | Residual stress determination using synchrotron X-ray diffraction

The high-energy X-ray diffraction experiments were performed at the Helmholtz-Zentrum Geesthach (HZG)-operated beamline High Energy Materials Science Beamline (HEMS) (P07B) at the synchrotron source PETRA III at Deutsches Elektron-Synchrotron with a photon energy of 87.1 keV and an incident beam size of 0.1×0.1 mm.[18] On the beamline, the specimens were positioned $\sim 1,500$ mm from a *Perkin Elmer XRD 1621* two-dimensional detector with a pixel size of $200 \times 200\ \mu m$ on a $2,048 \times 2,048$ X-ray sensitive array, permitting the acquisition of complete Debye–Scherrer diffraction rings in transmission. An illustration of the measurement set-up is shown in Figure 2.

Strain scanning was performed along two predefined paths. Path 1 was measured close to the surface, while Path 2 was located below the impact point of the specimen to assess the in-depth residual stress distribution, as illustrated in Figure 2d. Note that depth describes the vertical position starting at 0 mm from the location of the impact. The diffraction patterns, see Figure 2a, were azimuthally integrated within four sectors with a size of $\psi = 20°$ using the image processing software FIT2D.[19] An example of the resulting diffraction pattern is shown in Figure 2c. Results from the two sectors at 0° and 180° were averaged for determining strains parallel to the surface, from two sectors at 90° and 270° for transverse strains. However, in other work, the whole pattern has been utilized[20] instead of the four caked bins chosen in the present work. To quantify all sources of spatial distortion in the diffraction instrument a priori, a fiducial CeO_2 pattern in conjunction with a fitting routine described by Hammersley et al.[19,21] is used. A fit of the Al{311} reflection to a Pseudo-Voigt profile function over the integrated azimuthal angles was used to find the peak position from the one-dimensional diffraction pattern, representing the scattering angle $2\,\theta$. The Al{311} reflection was chosen to be the most statistically reliable data as it has the highest multiplicity of the experimentally observed reflections.[22] According to Clausen et al.[22] the Al{311} reflection responds almost linear to loadings and, therefore, constitutes a suitable reflection for characterization of macroscopic stress and strain by diffraction.

Knowledge of the unstrained (stress-free) lattice parameter is required to calculate the lattice strain from the shift in peak position[23] using

$$\varepsilon = \frac{\sin\theta_0}{\sin\theta} - 1, \tag{1}$$

where θ is the half scattered angle (Bragg angle) and θ_0 is the Bragg angle measured for the stress-free material. In this work, the diffraction angle θ_0 of the relaxed reference D-spacing is therefore determined by averaging the θ_0 values in a region (~ 15 mm away from the impact) that is assumed to be stress free. Measurements of the base material before impact showed a negligible stress level.

Residual stresses from X-ray diffraction data can be calculated either via a plane stress or via a plane strain assumption from elastic strains, see Appendix 2.3 for completeness. The error in the principal residual stress components $\Delta\sigma_{11}$ and $\Delta\sigma_{22}$ depends on the error $\Delta\theta_0$, $\Delta\theta_{11}$, and $\Delta\theta_{22}$ in the Bragg angle measured*. Using the law of error propagation and assuming a plane stress state as well as $\sin\theta \cong \sin\theta_0$ according to Pyzalla[23] yields

$$\Delta\sigma_{ii} = \frac{E}{1-\nu^2}\cot\theta_0\sqrt{[1+\nu]^2[\Delta\theta_0]^2 + [\Delta\theta_{ii}]^2 + \nu^2[\Delta\theta_{jj}]^2}, \tag{2}$$

with $ii = \{11, 22\}$ and $jj = \{22, 11\}$, respectively, where E represents the Young's modulus and ν the Poisson's ratio. Macroscopic values (E = 70 GPa and $\nu = 0.34$) instead of the lattice-dependent elastic constants of the Al{311} plane were used in the analysis, considering the nearly isotropic elastic behaviour of aluminium. The error of the principal strain components ε_{11} and ε_{22} can be expressed by[23]

$$\Delta\varepsilon_{ii} = \cot\theta_0\sqrt{\Delta\theta_0^2 + \Delta\theta_{ii}^2}\,. \tag{3}$$

Hereby, determined error bars are included in the plots of the experimental results.

*The Index 11 corresponds in the following to the stress/strain components in x-direction (longitudinal direction), where 22 represents the y-direction (normal/depth direction)

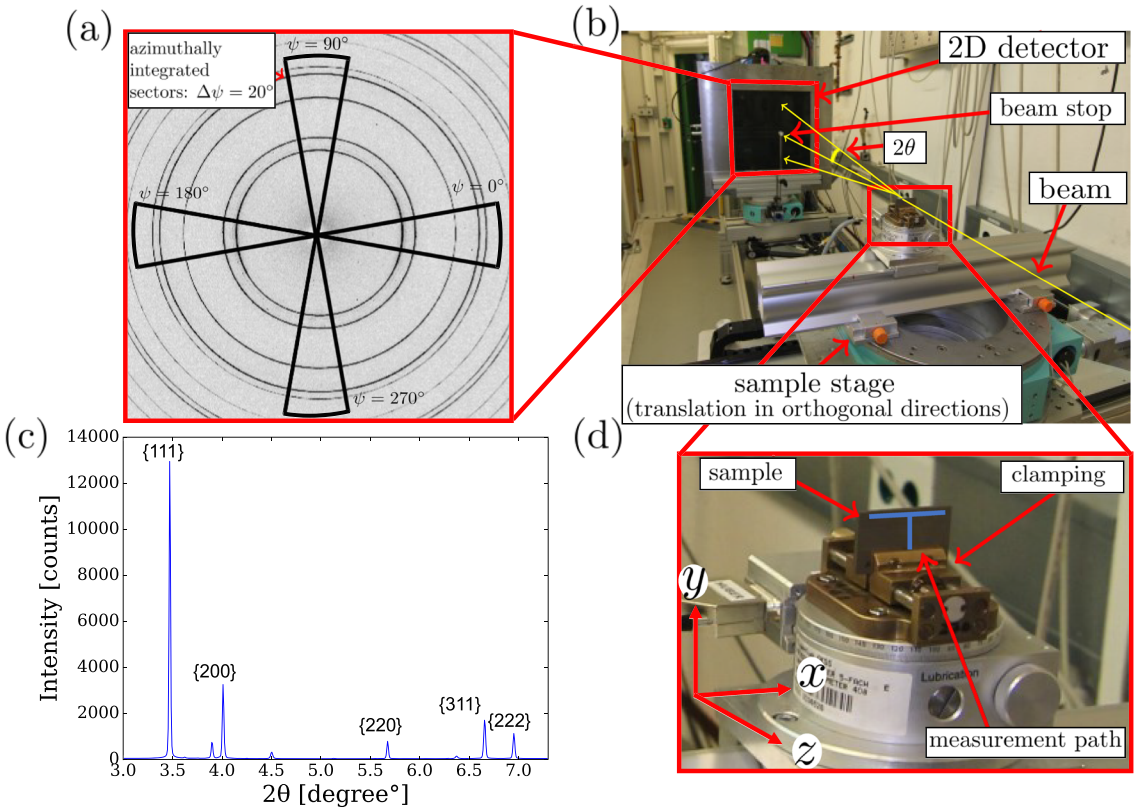

FIGURE 2 Measurement set-up at the P07B beamline, PETRA III - DESY (b), illustrating the diffraction data acquired (a) from specimens that had been subjected to single impact peening. Strain scanning was performed by moving the specimens (d) through the beam along two paths, indicated by the blue lines, and recording the position of the diffraction peaks for different specimen position. Using an area detector, the X-ray intensity at the intersection of the diffracted cone is acquired. (c) Example of the diffraction pattern after azimuthal integration

2.3 | Calculating residual stresses from elastic strains via plane stress and plane strain assumption

For the calculation of residual stresses from strains, one can assume a plane stress state in thin sheets, implying that the stress component parallel to the incoming beam is zero, that is, $\sigma_{33} = 0$. In this case, σ_{11} and σ_{22} can be expressed by[24]

$$\sigma_{ii} = \frac{E}{1-\nu^2}[\varepsilon_{ii} + \nu\varepsilon_{jj}], \tag{4}$$

with $ii = \{11, 22\}$ and $jj = \{22, 11\}$, respectively. The validity of this assumption is evaluated for different material thickness with the help of the FE model in Section 5.1.

Alternatively, one can assume a plane strain state, implying that the displacements of the material particles parallel to the incoming beam are assumed to be infinitesimal small. Therefore, σ_{11} and σ_{22} can be expressed by

$$\sigma_{ii} = [\lambda + 2G]\ \varepsilon_{ii} + \lambda\ \varepsilon_{jj}, \tag{5}$$

where λ as well as G are known as the Lamé constant and shear modulus, respectively. The stress σ_{33} can be calculated via $\sigma_{33} = \lambda\ [\varepsilon_{11} + \varepsilon_{22}]$.

3 | SIMULATION

3.1 | FE model

A dynamic three-dimensional FE model was set-up using ABAQUS/Standard to predict the residual stress distribution after a single peening. Figure 3 shows the FE model used, consisting of the specimen and impact ball. Since the process

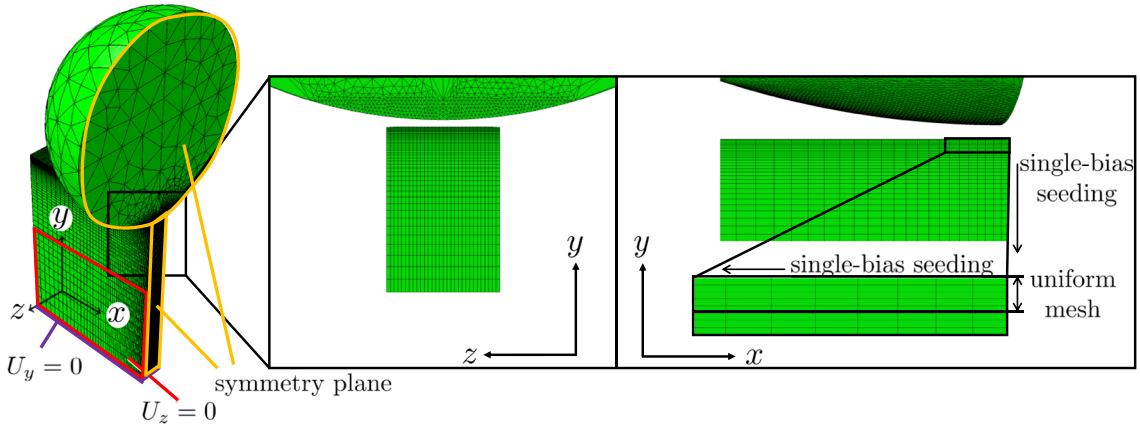

FIGURE 3 Three-dimensional FE model consisting of an aluminium specimen and a steel ball, assuming symmetry conditions along *yz*-plane. A smaller discretization is chosen near the impact region

is symmetric along the *yz*-plane, only half of the structure is modelled, applying corresponding symmetry boundary conditions. For the mesh discretization of the specimen, eight-node linear brick elements with reduced integration (C3D8R) were used where the ball is discretized via quadratic (10 nodes) tetrahedral elements (C3D10). The bottom of the specimen is constrained against displacements in the *y*-direction, and the sides at the lower end of the specimen (~ 12.5 mm) are constrained against displacement in *z*-direction, representing the boundary condition of the clamping during impact process (see Figure 1c). Before investigating the residual stresses, all displacement boundary conditions are removed to allow stress relaxation as present in the experiment as well. In the impact region, a minimum element size of $0.1 \times 0.1 \times 0.1$ mm is used. To provide a time and cost-efficient simulation, the element size is coarsened with increasing distance from the impact region. Convergence tests were conducted using different meshes to validate the adequacy of the current mesh discretization. Further, the time dependency of the simulation had been investigated to ensure that the duration of the relaxation phase lasts long enough to reach a nearly steady state. Based on the intended impact energy (0.25–1 J), the velocity is calculated from the kinetic energy and applied as initial velocity to the ball. Otherwise, gravity is neglected in the simulation. The contact is modelled based on a surface-to-surface contact with finite sliding considering normal hard and tangential frictionless contact. However, in Section 3.5, the influence of friction on the residual stresses has been investigated. Variations of the impact point in the experiment along the sample thickness (*z*-direction) can cause a slight change in the residual stress profile. Therefore, the exact indentation centre in the experiment caused by the single impact is determined and the impacting position adjusted accordingly in the FE simulation.

3.2 | Constitutive model

An isotropic linear elastic, viscoplastic material model is employed to account for the rate-dependent material behaviour during the impact. The Johnson–Cook model[25] is used to describe the rate-dependent plastic material behaviour, which is one of the most frequently used material models in impact studies.[26,27] The Johnson–Cook model consists of three parts, a strain hardening, a strain-rate strengthening, and a thermal softening part. The single impact process is assumed to be a purely mechanical process; therefore, temperature effects are neglected.[13,15,26] The reduced Johnson–Cook model determines the yield strength σ_y via

$$\sigma_y = [A + B \quad \varepsilon_P^n] \left[1 + C \ln\left(\frac{\dot{\varepsilon}_P}{\dot{\varepsilon}_{P,0}}\right)\right], \tag{6}$$

where ε_P is the equivalent plastic strain, $\dot{\varepsilon}_P$ the equivalent plastic strain rate, and $\dot{\varepsilon}_{P,0}$ the reference strain rate. The material constants A (static yield stress), B (strain hardening coefficient), C (strain rate hardening parameter), and n (strain hardening exponent) for AA5754 were taken from Smerd et al.[7] summarized in Table 2.

3.3 | Stress averaging

FE simulations deliver complex three-dimensional residual stress fields. The residual stress results from the residual stress determination via X-ray diffraction represent an averaged value within the cuboid gauge volume being defined by

TABLE 2 Johnson–Cook model parameters used for AA5754, taken from Smerd et al.[7] A Young's modulus of $E = 70$ GPa and a Poisson's ratio of $\nu = 0.34$ are assumed throughout this work

Material	Static yield stress, $A(MPa)$	Strain hardening coefficient, $B(MPa)$	Strain hardening exponent, n	Strain rate hardening parameter, C	Reference strain rate, $\dot{\varepsilon}_{P,0}$ (s^{-1})
AA5754	67.5	471.2	0.424	0.003	3.3e−3

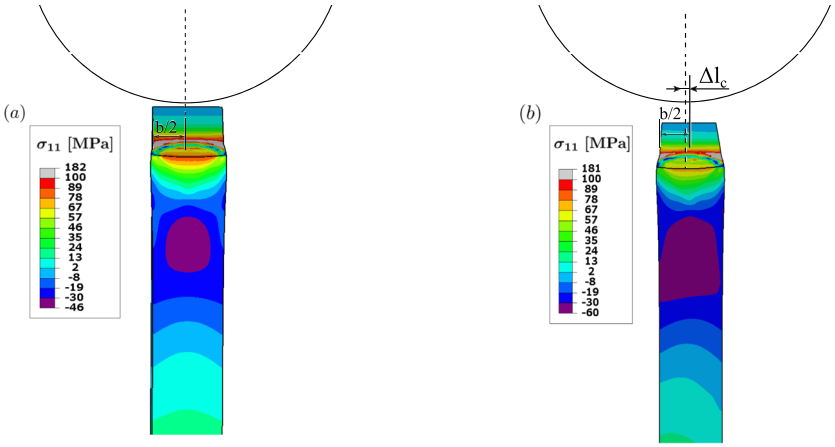

FIGURE 4 Residual stress distribution σ_{11} in the simulation for a middle cut of the sample for varying impact positions (a,b). Variation of the impact point leads to a minimal different residual stress profile. The impact point in (b) is varied by Δl_c=0.2 mm, which leads to a slight shift of the compressive stress region towards the opposite direction of the varied impact centre

the apertures of the beam. In order to compare simulation and X-ray diffraction measurements, nodal stresses† in the simulation are averaged within a volume as close as possible to the gauge volume ($0.1\times 0.1 \times 3$ mm) in the experiment at the different measurement locations to determine averaged residual stresses, see for example Keller et al.[13] The nodes in the model are selected based on their initial coordinates and thus, displacements due to the impact process are not considered. The displacements, especially in the area around the impact, may, therefore, lead to a minor deviation of the selected volumes between experiment and simulation.

3.4 | Influence of the impact position on the residual stress

Due to inaccuracies in the experimental set-up, the impact point in the experiment could not always be fully centred. The deviation of the actual impact position and the specimen centre is described by Δl_c as shown in Figure 4. This may lead to a slightly different residual stress profile characterized by a shift of the compressive stress region below the surface towards the opposite direction of the varied impact centre Δl_c (see Figure 4).

In order to estimate the influence of the varying impact point position on the residual stresses, different values for Δl_c (0.1, 0.2, and 0.3 mm) are investigated via simulation for an impact energy of 1 J. The values were chosen since 0.3 mm is the highest observed experimental deviation from the impact centre. Figure 5 depicts the spatially averaged stress at the surface (a) and in depth (b) for four different impact positions. A slight decrease in spatially averaged residual stress peak values is observed with an increasing distance to the centre, see Figure 5. However, otherwise, the influence of the impact position is determined as negligible.

3.5 | Influence of friction coefficient on the residual stress

The friction between the impacting ball and the specimen can have an effect on the residual stress.[28,29] However, the friction coefficient for this impact situation is unknown. To illustrate the influence of the friction coefficient during impact, a study on different friction coefficients reported for steel on aluminium (typically between 0.1 and 0.4)[30,31] has been conducted. Therefore, the tangential friction coefficient in the simulation was varied between frictionless up to a friction coefficient of $\mu = 0.45$. Only a minor influence on the averaged residual stress profiles around the impact in the near-surface region is determined as shown in Figure 6. Friction is not expected to have a significant influence in the present simulation since the ball does not rotate and the fact that the indentation of the ball is not very deep, only small relative movements are expected between sphere and material surface. In addition, friction did not have a significant influence on the loss of kinetic energy due to the impact for the friction coefficients investigated (increase of ∼0.5% com-

†At the surface, 155 nodes were averaged in each gauge volume.

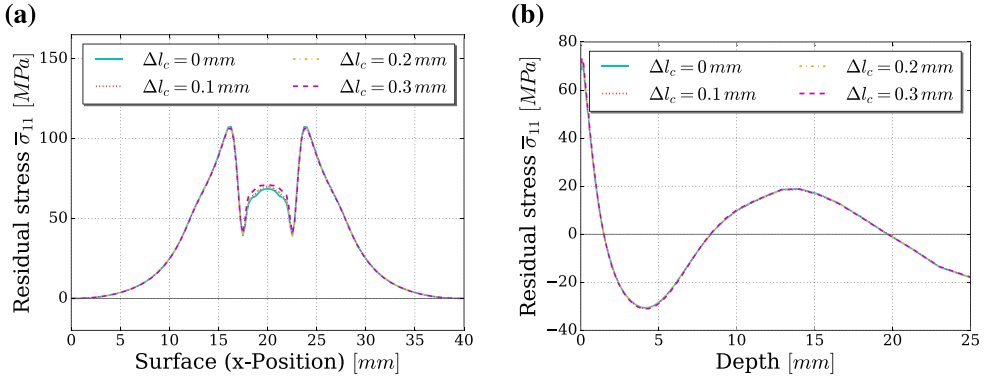

FIGURE 5 Course of spatially averaged residual stress $\overline{\sigma}_{11}$ (a) at the surface and (b) in depth for different impact positions along the thickness direction with distance Δl_c to the centre position. Only a minor influence on the averaged residual stress profiles is determined

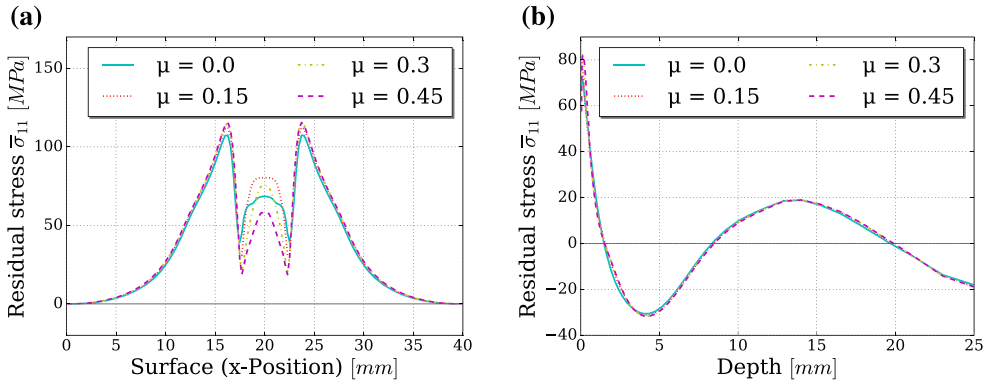

FIGURE 6 Residual stress $\overline{\sigma}_{11}$ (a) at the surface and (b) in depth for different friction coefficients at 1-J impact energy ranging from frictionless up to a friction coeffiecient of $\mu = 0.45$. Only a minor influence on the averaged residual stress profiles around the impact in the near-surface region is determined

paring the frictionless contact with a friction coefficient of 0.3 for 1 J). However, for different peening parameter and patterns, friction might have a more significant influence on the residual stress and the made assumption should always be considered. Therefore, in the following, the tangential contact is modelled as frictionless.

4 | VALIDATION OF SIMULATION BASED ON EXPERIMENTAL STRAIN AND ENERGY RESULTS

The current experimental results in terms of strains are used for validation of the simulation approach. Additionally, the loss of the impact energy, determined based on the back bouncing of the ball is used as additional rough comparison.

4.1 | Comparison of loss of kinetic energy

The impact energy is given by the chosen drop height of the ball with constant mass, that is, the potential energy of the ball. After the impact, the ball bounces back up again. The initial kinetic energy of the ball is converted into a dissipative part, leading in particular to plastic deformation within the specimen and an elastic part, where the stored strain energy leads to the back bouncing of the ball. The bouncing height after the impact was determined using a camera with an exposure time of 2 s, which allows determining the kinetic energy after the impact, see Aryaei et al.[32] for a similar approach. In

TABLE 3 Comparison of experimental and numerically determined percentage loss of kinetic energy of the ball after impact

Impact energy (J)	Energy loss simulation (%)	Energy loss experiment (%)
1	90.1	90.9
0.75	88.9	89.6
0.5	87.5	88.3
0.25	85.1	82.0

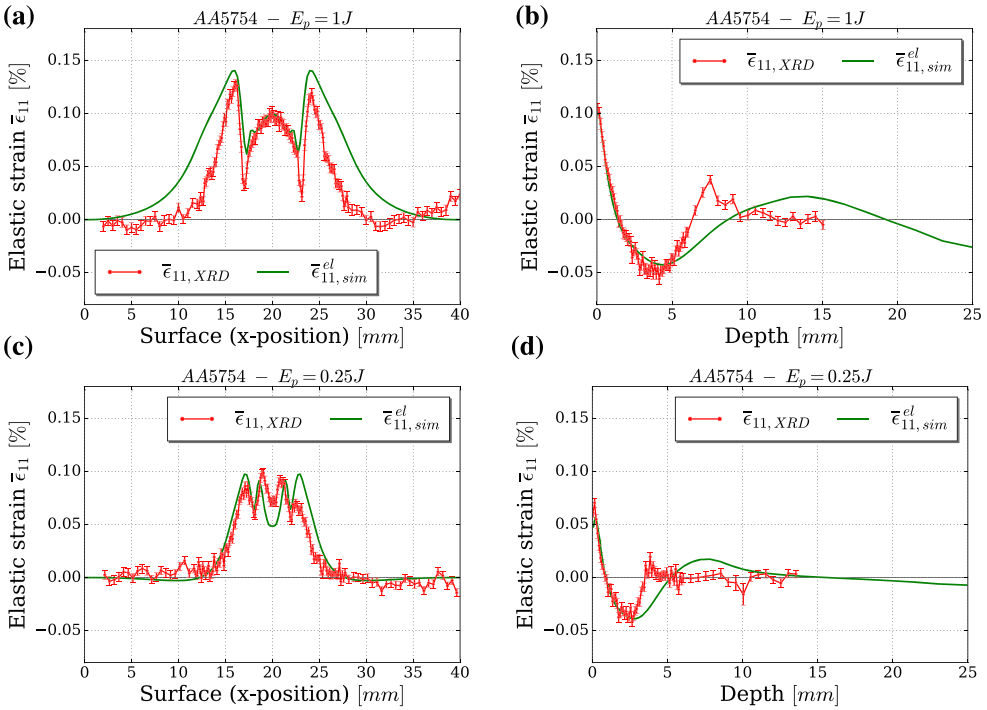

FIGURE 7 Comparison between measured $\bar{\varepsilon}_{11,XRD}$ and simulated $\bar{\varepsilon}^{el}_{11,sim}$ elastic strains after a single impact of AA5754 with a steel ball, for two different kinetic energies (1 J: (a,b); 0.25 J: (c,d)). Due to inaccuracies in the experimental set-up, the position was shifted by $\Delta l_z = 0.1$ mm. Note that depth describes the vertical position starting from 0 mm at the surface. Error bars indicate the experimental error calculated according to Equation 3

the simulation, the remaining kinetic energy after the impact is directly accessible. Table 3 depicts the percentage loss of kinetic energy due to the impact, which lies between 85% and 90% for the different impact energies. Experimental and numerical results show an excellent agreement in terms of the predicted energy loss of the ball due to the impact. Only for the lowest impact energy, a slight deviation between experiment and simulation is obtained.

4.2 | Comparison of experimentally and numerically determined elastic strains

The lattice strain is calculated from the diffraction angle θ of the experiment using Equation 1. The measured $\bar{\varepsilon}_{11,XRD}$ and simulated $\bar{\varepsilon}^{el}_{11,sim}$ elastic strains after single impact of AA5754 with the steel ball are compared in Figures 7 and 8. Here,

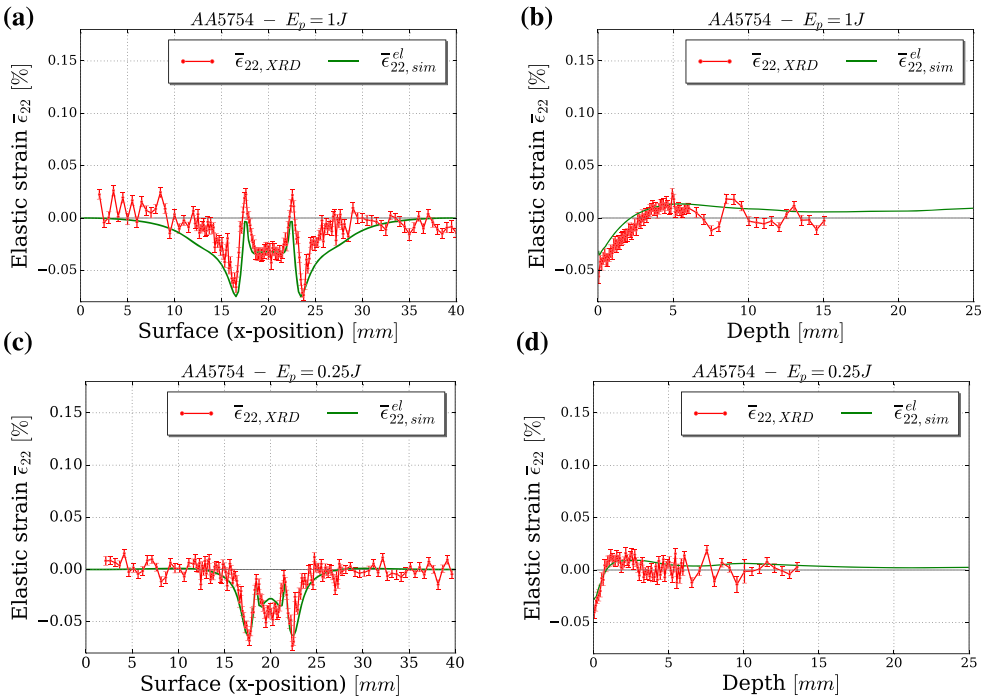

FIGURE 8 Comparison between measured $\bar{\varepsilon}_{22,XRD}$ and simulated $\bar{\varepsilon}^{el}_{22,sim}$ elastic strains after a single impact of AA5754 with a steel ball, for two different kinetic energies (1 J: (a,b); 0.25 J: (c,d)). The impact position was shifted by Δl_z=0.1 mm. Error bars indicate the experimental error calculated according to Equation 3

the strains along the surface as well as directly below the impact point in depth direction, corresponding to Paths 1 and 2 in the experimental set-up, see Figure 2d, are shown. Measurement of the samples before peening showed that the initial residual stress level is negligible compared to the peening-related induced stresses. Measured and simulated elastic strains are overall in good agreement; especially the maximum tensile strains match very well, only the width of the tensile strain zone is overestimated for the near-surface measurement path. Another slight difference is observed for instance for the depth of the compressive strains. One possible reason could be the proposed strain averaging methodology described in Section 3.3 since the nodes, which are selected for averaging purposes, are selected based on the undeformed state. Thus, the difference between the measured gauge volume and the averaged volume in the simulation is largest within the impact region. The comparison of the strains in the y-direction $\overline{\varepsilon}_{22,XRD}$ and $\overline{\varepsilon}^{\,el}_{22,sim}$ also reveals a general good agreement despite fluctuations of the experimentally observed strains at larger depth, see Figure 8. The comparison for the further impact energies (0.5 and 0.75 J) also show similar agreements.

Overall, the strain distribution between experiment and simulation are in qualitative accordance, serving as a valid basis for the subsequent comparison of the residual stresses as presented in the following section.

5 | DETERMINATION OF RESIDUAL STRESS FIELDS

5.1 | Evaluation of plane stress and plane strain assumption based on numerical results

From the simulation, the three-dimensional stress state is directly available. However, in the experiments, the near-surface and in-depth elastic strains have to be used to calculate residual stresses by using either a plane stress or a plane strain

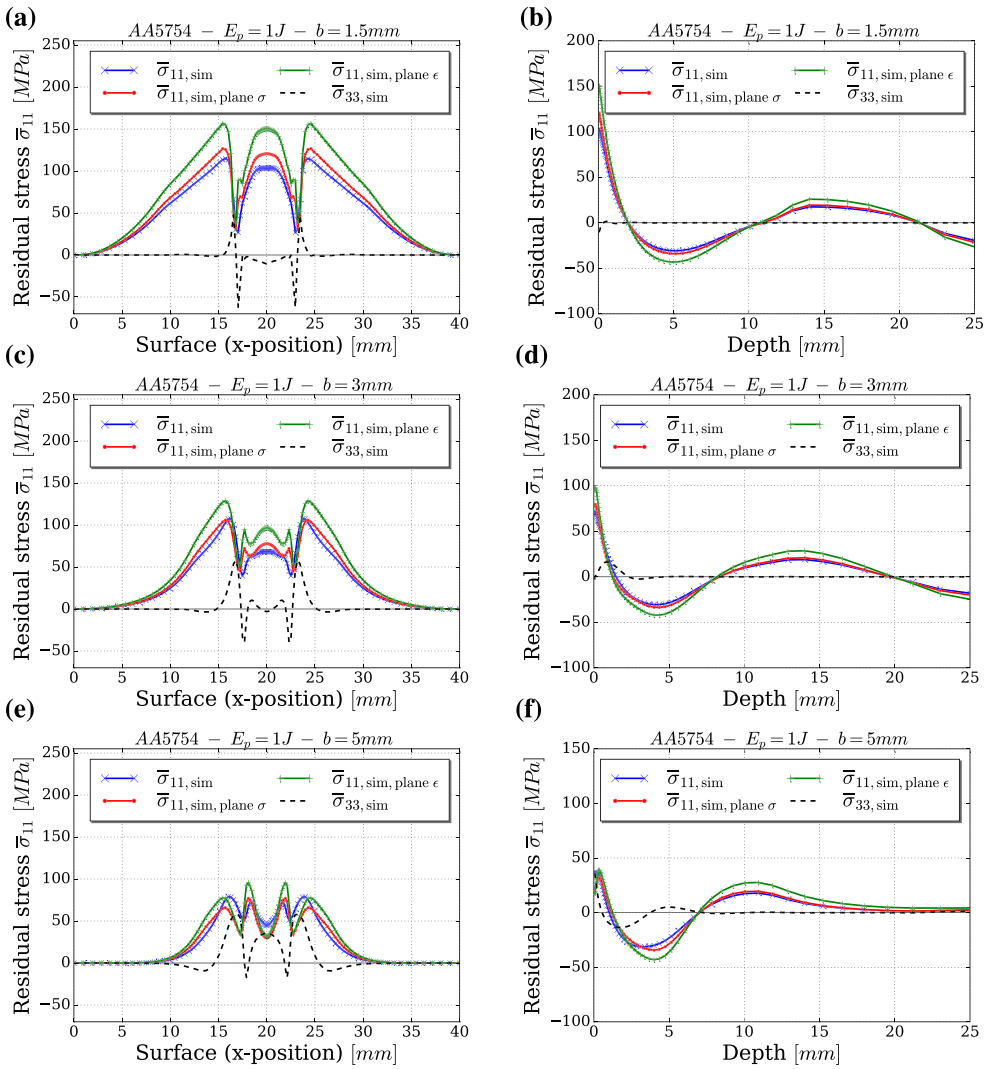

FIGURE 9 Comparison of simulation results for residual stress distribution, resulting from full three-dimensional calculation $\overline{\sigma}_{11,sim}$ and $\overline{\sigma}_{33,sim}$ or calculated from resulting elastic strains $\overline{\varepsilon}^{\,el}_{11,sim}$ and $\overline{\varepsilon}^{\,el}_{22,sim}$ assuming plane stress $\overline{\sigma}_{11,sim,plane\ \sigma}$ or plane strain $\overline{\sigma}_{11,sim,plane\ \epsilon}$ conditions. The results are shown for three different specimen thicknesses: b = 1.5 mm (a,b), b = 3 mm (c,d) as well as b = 5 mm (e,f). $\overline{\sigma}_{33,sim}$ is shown for completeness. It can be concluded that the plane stress assumption is the more adequate approximation for relatively thin specimens of the alloy AA5754

assumption. The stress calculation based on both assumptions are summarized for completeness in Section 2.3. To investigate the effect of these assumptions on the resulting residual stresses in detail, the simulation results for the elastic strain components $\overline{\varepsilon}^{el}_{11,sim}$ and $\overline{\varepsilon}^{el}_{22,sim}$ (Figure 7) are used to calculate the resulting stresses based on the plane stress or plane strain assumption, see Figure 9. It can be seen that for the investigated specimen thickness of 3 mm, only a slight deviation between the stress component $\overline{\sigma}_{11,sim}$ of the three-dimensional simulation and the stress calculated based on the plane stress assumption $\overline{\sigma}_{11,sim,plane\ \sigma}$ is visible. The stress $\overline{\sigma}_{11,sim,plane\ \varepsilon}$, assuming plane strain conditions, shows a significant difference to the full three-dimensional simulation results, indicating clearly that plane stress is the more appropriate assumption compared to plane strain for the thickness investigated. Apart from this, specimens with a thickness of 1.5 and 5 mm, representing typical sheet thicknesses for applications, are used in order to investigate these assumptions further. Consistent with the previous observation, the full field results for a thickness of 1.5 mm agree well with the plane stress results. For a thickness of 5 mm, the plane stress results show an increasing deviation to the full three-dimensional stress state, indicating that the plane stress assumption does not longer hold for a further increasing thickness. Still, the plane strain assumption leads to even larger differences. Additionally, the stress component in thickness direction from the simulation is shown. Plane stress conditions assume that this component should be comparably small. Consequently, the stress component can be an indicator for possible deviations between experiment and simulation results. For completeness, the effect of the plane stress and plane strain assumption on the residual stress component σ_{22} is analysed in Appendix A. Since σ_{22} should be vanishing at the surface, a comparatively larger deviation than for σ_{11} is present for both assumptions. Still for in depth direction, the plane stress assumption shows an acceptable agreement.

Based on this numerical investigation, it can be concluded that the plane stress assumption seems a much more adequate approximation for relatively thin specimens (up to 3 mm) of the alloy AA5754 compared to a plane strain assumption.

5.2 | Residual stress comparison between experiment and simulation

Based on the previous results, the resulting residual stresses are calculated assuming a plane stress state based on the experimentally measured strains, see Figures 7 and 8. The residual stress results near the surface show that the single impact with 1 J in AA5754 induces a maximum tensile stress tensile stress of 100 MPa on both sides of the impact centre, see Figure 10a. Additionally, tensile stresses in the impact centre are observed, ranging up to 70 MPa. The agreement

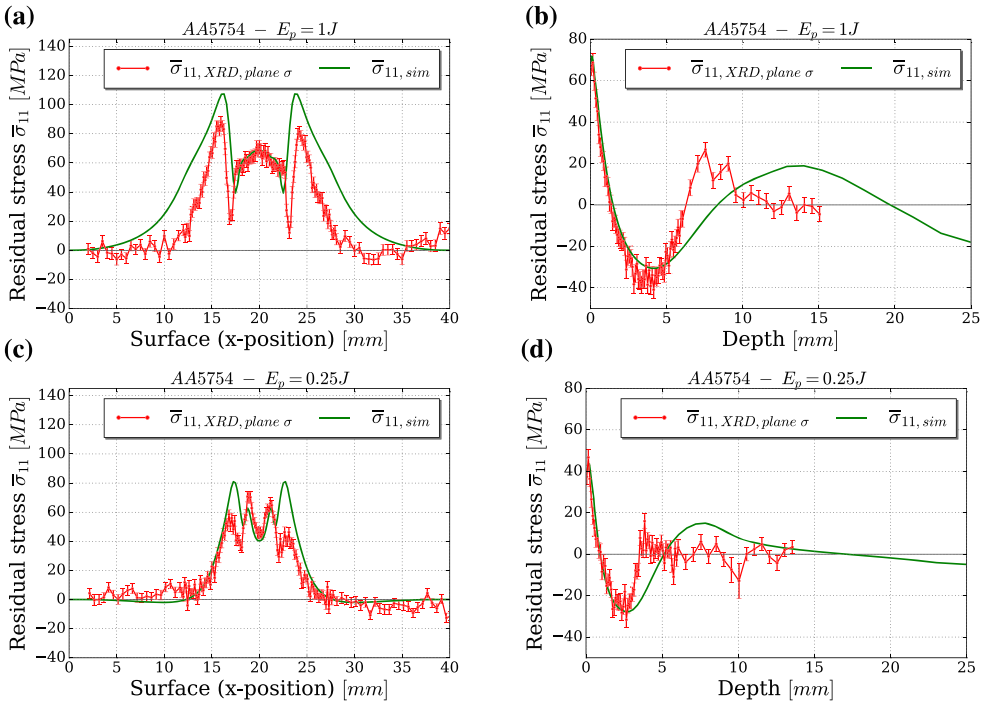

FIGURE 10 Comparison between experimentally determined $\overline{\sigma}_{11,XRD,plane\ \sigma}$ and simulated $\overline{\sigma}_{11,sim}$ residual stresses after single impact of AA5754 with a steel ball, for two different kinetic energies (1 J: (a,b); 0.25 J: (c,d)). Error bars indicate the experimental error calculated according to Equation 2. The measured residual stresses $\overline{\sigma}_{11,XRD,plane\ \sigma}$ were calculated based on the plane stress assumption

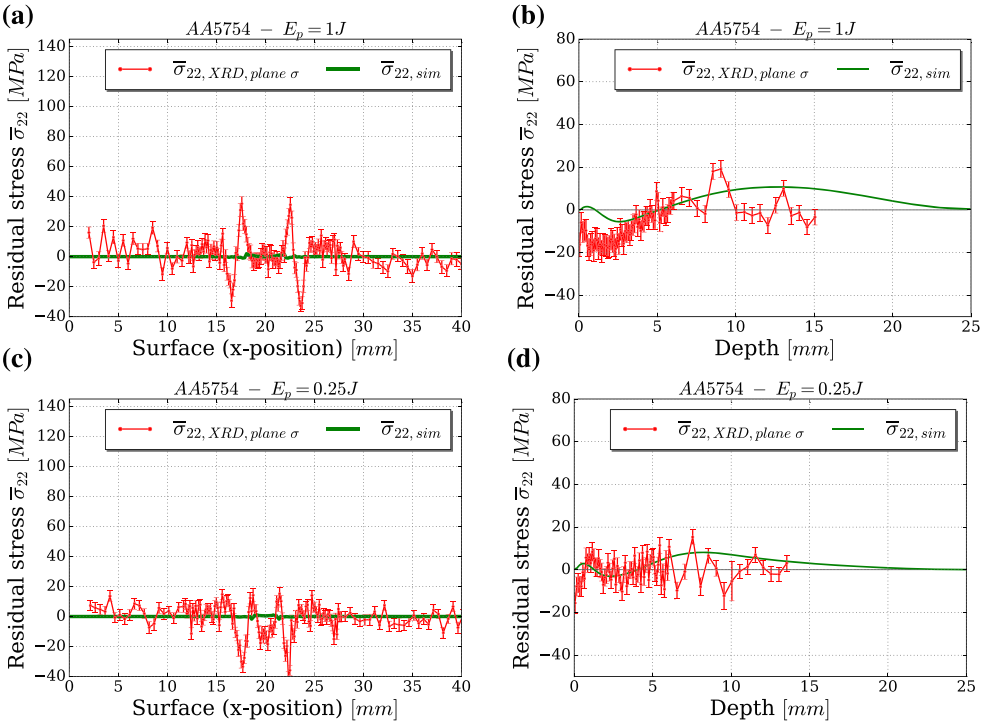

FIGURE 11 Comparison between measured $\overline{\sigma}_{22,XRD,plane\ \sigma}$ and simulated $\overline{\sigma}_{22,sim}$ residual stresses after single impact for AA5754 with a steel ball, for two different kinetic energies (1 J: (a,b); 0.25 J: (c,d)). Error bars indicate the experimental error calculated according to Equation 2. The measured residual stresses $\overline{\sigma}_{22,XRD,plane\ \sigma}$ were calculated based on the plane stress assumption

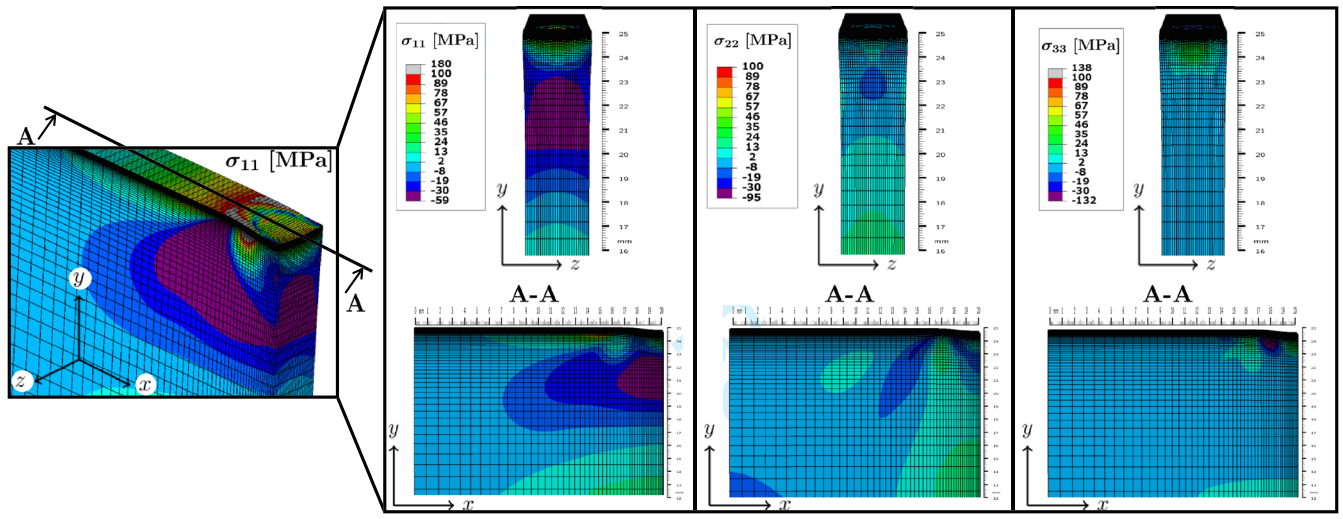

FIGURE 12 Three-dimensional residual stress field of AA5754 for a single impact on a specimen with a thickness of 3 mm with an impact energy of 1 J. The results indicate beneficial compressive residual stresses below the surface for σ_{11}

between measurement and simulation is in general good. Below the surface of the AA5754 specimen, there is a distinct maximum of compressive residual stresses, followed by smaller compensating tensile stresses at larger depth, Figure 10b. The simulation correctly predicts the maximum compressive residual stress at the same depth as observed experimentally. However, with increasing depth, the residual stresses decrease steeper in the experiment compared to the simulation, as observed already in the comparison of the strains.

For an impact energy of 0.25 J, the results are similar compared to an impact with an energy of 1 J, but the width of the tensile stress region is smaller, their tensile stress maxima are lower, and the compressive stress maximum in depth is also

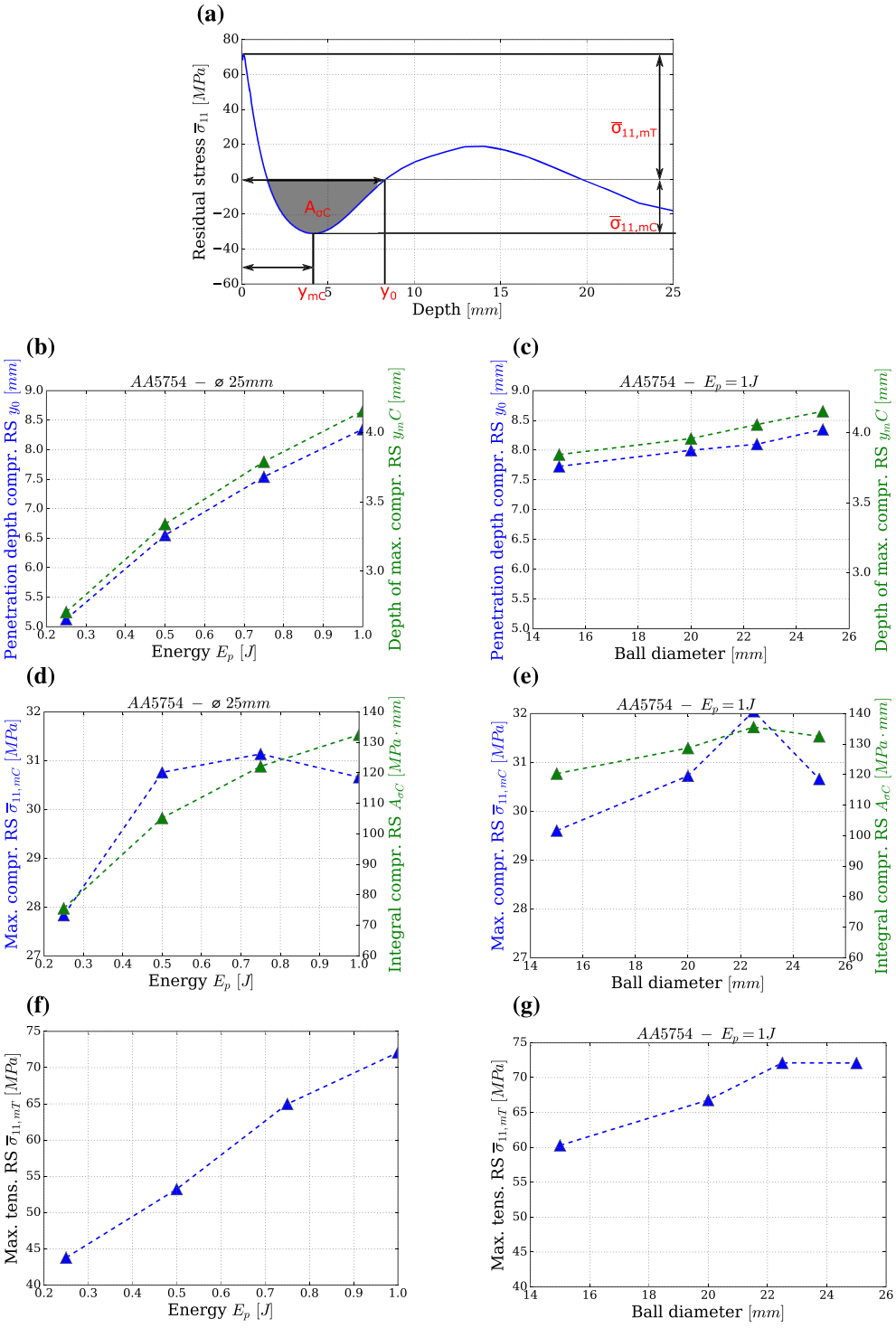

FIGURE 13 Effect of varying the impact energy (b,d,f) and the ball size (c,e,g) on characteristic values (a) of the residual stress profile. (b,c) Resulting penetration depth of the compressive residual stresses y_0 and depth of maximum compressive stresses y_{mC}; (d,e) integral of the compressive residual stress area $A_{\sigma C}$ together with the maximum compressive residual stresses $\overline{\sigma}_{11,mC}$; (f,g) effect on the maximum tensile stresses $\overline{\sigma}_{11,mT}$

considerably smaller (Figure 10c,d). However, overall experiment and simulation agree well. For the stress component $\overline{\sigma}$ further investigated energies, a comparable agreement between experiment and simulation is observed, see Figure 11 and Appendix B.

5.3 | Influence of impact parameters on resulting residual stress profiles

The evaluation has shown that the results of the FE model agree overall well with the experimental results for AA5754 sheets of 3 mm thickness, accounting in particular for the underlying assumption in the experiment and simulation. Thus,

the influence of the different (process) parameters of a single impact can be analysed based on the full three-dimensional FE simulation. The impact results in a complex residual stress field with a distinct compressive maximum at a certain depth underneath the impact, see Figure 12. Counterbalancing tensile stresses are in particular present close to the surface. For a real application purpose, the impact energy (and the number of impacts) has to be adjusted such that significant compressive stresses are created as well as that low tensile stresses are only present in uncritical regions. Otherwise, those tensile stresses will increase the risk of crack initiation and accelerated crack propagation in industrial applications.

The effect of the parameter, impact energy, and ball size on the residual stress profile, has been assessed in a numerical study by analysing the following characteristic values (see Figure 13a):

- Penetration depth of compressive residual stress y_0 .
- Depth of maximum compressive residual stress y_{mC} .
- Maximum compressive residual stress $\overline{\sigma}_{11,mC}$.
- Maximum tensile residual stress $\overline{\sigma}_{11,mT}$.
- Integral over compressive residual stress $A_{\sigma C}$. ‡

These characteristic parameters are expected to be relevant for the fatigue performance.[33–35] In the following, the impact energy is varied by changing the impact velocity. Further, the influence of the ball diameter is investigated by varying the ball thickness at constant density and impact energy by adjusting the impact velocity as well.

The simulation results show that an increase in the initial ball velocity and hence kinetic impact energy causes a significant increase in the penetration depth of compressive residual stresses y_0, the integral compressive residual stress area $A_{\sigma C}$, as well as depth y_{mC} and tensile $\overline{\sigma}_{11,mT}$ residual stresses, see Figure 13b,d,f. A variation in the ball size with the same density and kinetic energy leads to less significant changes in the residual stress characteristics, see Figure 13c,e,g. Still, an increase in diameter of the ball at constant density and impact energy results in an increase of depth (y_0 and y_{mC}) and maximum tensile stress $\overline{\sigma}_{11,mT}$, see Figure 13c,g. The observed dependencies of the varied ball velocity and size agree well with results in literature for ultrasonic impact treatment where the pin velocity and pin size causes the changes of the parameters investigated.[15] It can be concluded that the investigated ball size at constant impact energy has only minor influence on the resulting residual stress field.

6 | CONCLUSION

The elementary process of mechanical peening, represented by a single-impact test, has been studied by a combined experimental–numerical approach in terms of the resulting residual stress fields. For this purpose, high energy X-ray diffraction and three-dimensional FE simulations have been used. The validated numerical analysis can assist in providing a further understanding of the single impact process. The effect of single impact parameters, such as energy and the ball size, has been exemplary analysed. The following results have been obtained:

- The plane stress assumption seems an adequate approximation for the relatively thin specimens (up to 3 mm) of the alloy AA5754. For thicker specimens, an increasing deviation in comparison to the three-dimensional stress state directly available from the simulation is observed. However, the plane stress assumption is still more appropriate compared to assuming plane strain conditions.
- Simulated and measured residual stress profiles are in good agreement for the residual stress profile at the surface; in-depth, an agreement up to the point of maximum compressive residual stress is observed.
- The impact creates a compressive residual stress field at a certain depth underneath the impact that is balanced by tensile stresses close to the surfaces.
- The maximum compressive stresses depend on the energy of the impact. An increase in impact energy causes an increase in penetration depth of compressive residual stresses as well as depth and magnitude of maximum compressive residual stresses.

‡This residual stress area is defined as the closest compressive stress area near the surface. Residual stresses at deeper depth are not considered relevant for evaluating the performance.

NOMENCLATURE

A	static yield strength
$A_{\sigma C}$	integral over compressive residual stress
B	strain hardening coefficient
C	strain rate hardening parameter
E	macroscopic Young's modulus
G	shear modulus
b	thickness of specimen
n	strain hardening exponent
y_0	penetration depth of compressive residual stress
y_{mC}	depth of maximum compressive residual stress
Δl_c	distance between impact centre and specimen midthickness
λ	Lamé constant
μ	friction coefficient
ν	Poisson's ratio
ψ	azimuthal angle on the diffraction cones
$\Delta\varepsilon$	error in measured elastic strain
$\dot{\varepsilon}_P$	equivalent plastic strain rate
$\dot{\varepsilon}_{P,0}$	reference strain rate
$\overline{\varepsilon}_{ii,XRD}$	lattice strain
$\overline{\varepsilon}^{el}_{ii,sim}$	elastic strain obtained in the simulation
ε_P	equivalent plastic strain
$\Delta\sigma$	error in the experimentally determined residual stress
$\overline{\sigma}_{11,mC}$	maximum compressive residual stress
$\overline{\sigma}_{11,mT}$	maximum tensile residual stress
σ_y	yield strength
$\overline{\sigma}_{ii,sim,plane\ \sigma}$	calculated residual stresses from lattice strain assuming plane stress
$\overline{\sigma}_{ii,sim,plane\ \varepsilon}$	calculated residual stresses from lattice strain assuming plane strain
$\overline{\sigma}_{ii,sim}$	averaged residual stress obtained in the simulation
$\Delta\theta$	measurement error of the scattering angle
θ	half scattered angle
θ_0	half scattered angle of the stress-free material

ACKNOWLEDGEMENTS

We acknowledge Deutsches Elektronen-Synchroton (DESY), Germany, for the provision of the synchrotron radiation facilities at beamline P07B of Helmholtz-Zentrum Geesthacht. This research did not receive any specific grant from funding agencies in the public, commercial, or not-for-profit sectors.

ORCID

Paul Sandmann https://orcid.org/0000-0002-3656-5324
Emad Maawad https://orcid.org/0000-0003-4500-2301
Benjamin Klusemann https://orcid.org/0000-0002-8516-5087

REFERENCES

[1] I. E. Kopsov, *Int. J. Fatigue* **1991**, *13*(6), 479.
[2] C. A. Rodopoulos, S. A. Curtis, E. R. De los Rios, J. Solis Romero, *Int. J. Fatigue* **2004**, *26*(8), 849.
[3] S. Keller, M. Horstmann, N. Kashaev, B. Klusemann, *Int. J. Fatigue* **2019**, *124*, 265.
[4] S. Roy, J. W. Fisher, B. T. Yen, *Int. J. Fatigue* **2003**, *25*(9-11), 1239.
[5] V. Schulze, *Modern mechanical surface treatment: States, stability, effects*, Hoboken, New Jersey, USA: John Wiley & Sons; **2006**.

[6] L. Hacini, N. Van Lê, P. Bocher, *J. Mater. Proc. Technol.* **2008**, *208*(1-3), 542.
[7] R. Smerd, S. Winkler, C. Salisbury, M. Worswick, D. Lloyd, M. Finn, *Int. J. Impact Eng.* **2005**, *32*(1-4), 541.
[8] S. A. Meguid, G. Shagal, J. C. Stranart, *Int. J. Impact Eng.* **2002**, *27*(2), 119.
[9] T. Kim, J. H. Lee, H. Lee, S. Cheong, *Materials Design* **2010**, *31*(1), 50.
[10] T. Hong, J. Y. Ooi, B. Shaw, *Eng. Failure Anal.* **2008**, *15*(8), 1097.
[11] T. Chaise, J. Li, D. Nélias, R. Kubler, S. Taheri, G. Douchet, V. Robin, P. Gilles, *J. Mater. Proces. Technol.* **2012**, *212*(10), 2080.
[12] R. A. Brockman, W. R. Braisted, S. E. Olson, R. D. Tenaglia, A. H. Clauer, K. Langer, M. J. Shepard, *Int. J. Fatigue* **2012**, *36*(1), 96.
[13] S. Keller, S. Chupakhin, P. Staron, E. Maawad, N. Kashaev, B. Klusemann, *J. Mater. Proces. Technol.* **2018**, *255*, 294.
[14] B. L. Boyce, X. Chen, J. W. Hutchinson, R. O. Ritchie, *Mech. Mater.* **2001**, *33*(8), 441.
[15] C. Guo, Z. Wang, D. Wang, S. Hu, *Appl. Surface Sci.* **2015**, *347*, 596.
[16] X. Xiao, X. Tong, Y. Liu, R. Zhao, G. Gao, Y. Li, *Int. J. Mech. Sci.* **2018**, *137*, 182.
[17] M. Froend, V. Ventzke, S. Riekehr, N. Kashaev, B. Klusemann, J. Enz, *Mater. Charac.* **2018**, *143*, 59.
[18] N. Schell, A. King, F. Beckmann, T. Fischer, M Müller, A. Schreyer, in Mater. Sci. Forum. Hoboken, New Jersey, USA. *772* **2014**, 57–61.
[19] A. P. Hammersley, FIT2D V9.129 Reference Manual V3.1, ESRF Internal Report, ESRF98HA01T, **1998**.
[20] D. Schnubel, M. Horstmann, V. Ventzke, S. Riekehr, P. Staron, T. Fischer, N. Huber, *Mater. Sci. Eng. A* **2012**, *546*, 8.
[21] A. P. Hammersley, S. O. Svensson, A. Thompson, *Nuclear Inst. Methods Phys. Res. Sect. A: Accelerators, Spectrometers, Detectors and Associated Equipment* **1994**, *346*(1-2), 312.
[22] B. Clausen, T. Lorentzen, T. Leffers, *Acta Materialia* **1998**, *46*(9), 3087.
[23] A. Pyzalla, *J. Neutron Res.* **2000**, *8*(3), 187.
[24] P. Staron, A. Schreyer, H. Clemens, S. Mayer, *Neutrons and synchrotron radiation in engineering materials science: From fundamentals to applications*, Hoboken, New Jersey, USA: John Wiley & Sons **2017**.
[25] G. R. Johnson, in Proc. 7th Inf. Sympo. Ballistics. Hoboken, New Jersey, USA. **1983**, 541.
[26] H. Dianyin, G. Ye, M. Fanchao, S. Jun, W. Yanfei, R. Mengxi, W. Rongqiao, *Chin. J. Aeronautics* **2017**, *30*(4), 1592.
[27] F. J. Zerilli, R. W. Armstrong, *J. Appl. Phys.* **1987**, *61*(5), 1816.
[28] J. Schwarzer, V. Schulze, O. Vohringer, Proc. Int. Conf. Shot Peening, *8* **2002**.
[29] G. H. Majzoobi, R. Azizi, A. A. Nia, *J. Mater. Proces. Technol.* **2005**, *164*, 1226.
[30] B. Sanborn, B. Song, E. Nishida, *Experimental Mech.* **2018**, *58*(2), 335.
[31] D. Fuller, 2d. coefficients of friction.
[32] A. Aryaei, K. Hashemnia, K. Jafarpur, *Int. J. Impact Eng.* **2010**, *37*(10), 1037.
[33] C. Correa, L. R. de Lara, M. Díaz, J. A. Porro, A. García-Beltrán, J. L. Ocaña, *Int. J. Fatigue* **2015**, *70*, 196.
[34] S. Chupakhin, B. Klusemann, N. Huber, N. Kashaev, *Int. J. Adv. Manuf. Tech.* **2019**, *102*(2019), 1567.
[35] S. Curtis, E. R. De los Rios, C. A. Rodopoulos, A. Levers, *Int. J. Fatigue* **2003**, *25*(1), 59.

How to cite this article: Sandmann P, Nielsen M-A, Keller S, Maawad E, Staron P, Klusemann B. Combined experimental-numerical study on residual stresses induced by a single impact as elementary process of mechanical peening. *Strain*. 2020;56:e12338. https://doi.org/10.1111/str.12338

APPENDIX A: NUMERICALLY DETERMINED STRESSES COMPARING PLANE STRESS AND PLANE STRAIN ASSUMPTION FOR $\sigma 22$

In addition to the investigation conducted in Section 5.1, the simulation results for the elastic strain components $\overline{\varepsilon}_{11}^{el}$ and $\overline{\varepsilon}_{22}^{el}$ (Figure 7) are also used to calculate the stresses based on both assumptions, plane stress and plane strain for the averaged stresses in y-direction ($\overline{\sigma}_{22}$), see Figure A1. It can be observed that $\overline{\sigma}_{33}$ is comparetively larger than $\overline{\sigma}_{22}$ leading to a deviation of the result where $\overline{\sigma}_{33}$ is significant. Thus, the relative error of the residual stress obtained by the simulation compared to the X-ray diffraction measurements computed with a plane stress assumption increases.

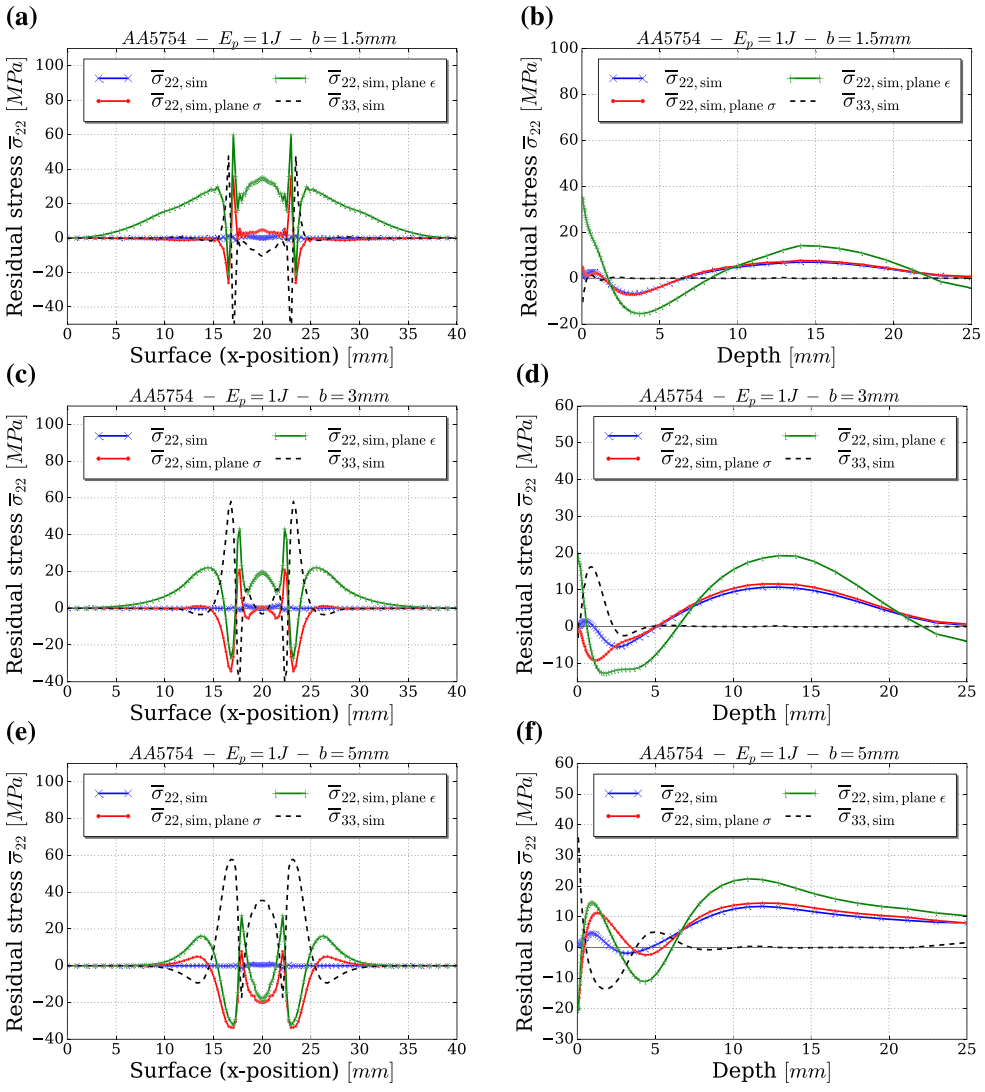

FIGURE A1 The elastic strains extracted from the simulation were used to calculate the residual stresses by assuming either plane stress $\overline{\sigma}_{22,sim,plane\ \sigma}$ or plane strain $\overline{\sigma}_{22,sim,plane\ \epsilon}$ for a sheet with a thickness b = 1.5 mm (a,b), b = 3 mm (c,d) as well as b = 5 mm (e,f). Additionally, the direct simulation results from the three-dimensional calculation for the stress components $\overline{\sigma}_{22,sim}$ and $\overline{\sigma}_{33,sim}$ are shown

APPENDIX B : RESIDUAL STRESS COMPARISON BETWEEN EXPERIMENT AND SIMULATION FOR 0.5 J AND 0.75 J

For completeness, the experimental–numerical comparison in terms of the residual stresses for the energies 0.75 and 0.5 J is shown in Figure B2 for $\overline{\sigma}_{11}$ and $\overline{\sigma}_{22}$, respectively.

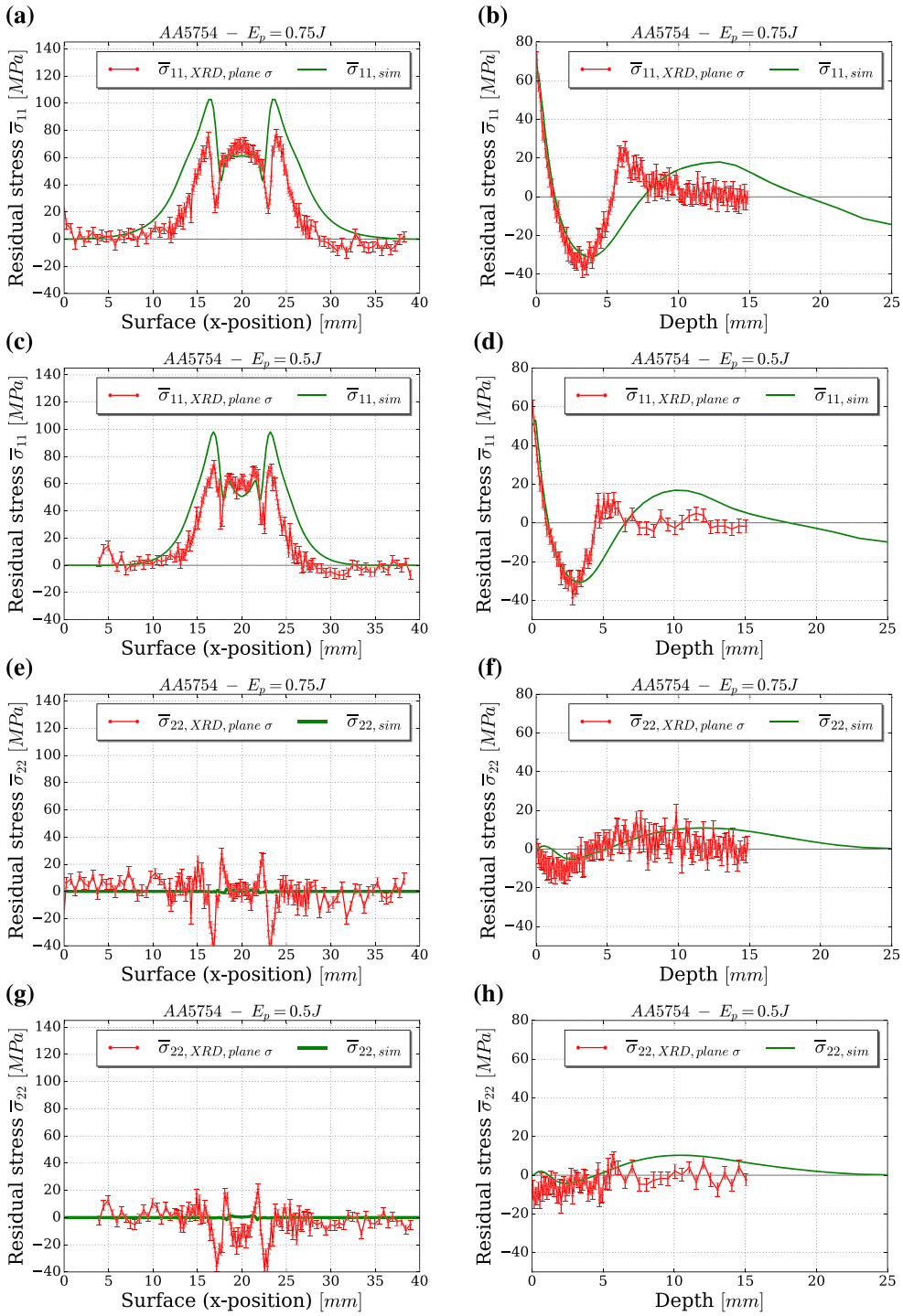

FIGURE B2 Comparison between measured $\overline{\sigma}_{ii,XRD,plane\ \sigma}$ and simulated $\overline{\sigma}_{ii,sim}$ residual stresses after single impact for AA5754 with a ball diameter of 25 mm. The measured residual stresses $\overline{\sigma}_{11,XRD,plane\ \sigma}$ were calculated based on the plane stress assumption